Electron Transfer from Encapsulated Fe 3 C to the Outermost Ndoped Carbon Layer for Superior ORR

Javier Quílez-Bermejo, Ayoub Daouli, Sergio García Dalí, Yingdan Cui, Andrea Zitolo, Jimena Castro-Gutiérrez, Mélanie Emo, Maria Izquierdo, William Mustain, Michael Badawi, et al.

To cite this version:

Javier Quílez-Bermejo, Ayoub Daouli, Sergio García Dalí, Yingdan Cui, Andrea Zitolo, et al.. Electron Transfer from Encapsulated Fe 3 C to the Outermost Ndoped Carbon Layer for Superior ORR. Advanced Functional Materials, inPress, 10.1002/adfm.202403810 . hal-04573050

HAL Id: hal-04573050
https://hal.univ-lorraine.fr/hal-04573050v1

Submitted on 13 May 2024

Electron Transfer from Encapsulated Fe_3C to the Outermost N-doped Carbon Layer for Superior ORR

Javier Quílez-Bermejo[1,*], Ayoub Daouli[2], Sergio García Dalí[1,3], Yingdan Cui[4,5], Andrea Zitolo[6], Jimena Castro-Gutiérrez[1], Mélanie Emo[7], Maria T. Izquierdo[8], William Mustain[4], Michael Badawi[2,9], Alain Celzard[1,10], Vanessa Fierro[1,*].

[1]Université de Lorraine, Centre National de la Recherche Scientifique (CNRS), Institut Jean Lamour (IJL), F-88000, Épinal, France.

[2]Université de Lorraine, CNRS, Laboratoire de Physique et Chimie Théoriques (LPCT), F-54000 Nancy, France.

[3]Departamento de Ciencia de los Materiales e Ingeniería Metalúrgica, Universidad de Oviedo, 33004, Oviedo, Spain.

[4]Department of Chemical Engineering, University of South Carolina, Columbia, SC United States of America.

[5]Department of Chemical and Biological Engineering, The Hong Kong University of Science and Technology, Kowloon, Hong Kong, China.

[6]Synchrotron SOLEIL, Départementale 128, 91190 Saint Aubin, France.

[7]Université de Lorraine, Institut Jean Lamour (IJL), 54011 Nancy, France.

[8]Instituto de Carboquímica (ICB-CSIC), Miguel Luesma Castán 4, E-50018, Zaragoza, Spain.

[9]Université de Lorraine, CNRS, Laboratoire Lorrain de Chimie Moléculaire (L2CM), F-57000 Metz, France.

[10]Institut Universitaire de France (IUF), F-75231 Paris, France.

Abstract

Encapsulating Fe_3C in carbon layers has emerged as an innovative strategy for protecting Fe_3C while preserving its high oxygen reduction activity. However, fundamental questions persist regarding the active sites of encapsulated Fe_3C due to the restricted accessibility of oxygen molecules to the metal sites. Herein, we unveil the intrinsic electron transfer mechanisms of Fe_3C nanoparticles encapsulated in N-doped carbon materials for oxygen reduction electrocatalysis. We used the precision-structured C_1N_1 material to synthesize N-doped carbons with encapsulated Fe_3C, significantly enhancing catalytic activity (E_{ONSET} = 0.98 V) and achieving near-100 % operational stability. In anion-exchange membrane fuel cells, an excellent peak power density of 830 mW·cm^{-2} was reached at 60 °C. Our experimental and computational results revealed that the presence of Fe_3C cores dynamically triggers electron transfer to the outermost carbon layer. This phenomenon amplifies the oxygen reduction reaction performance at N sites, contributing significantly to the observed catalytic enhancement.

Keywords

C_1N_1, Fe_3C, encapsulation in N-doped carbon, oxygen reduction reaction, electron transfer

Introduction

The substantial reliance of our global economy on fossil fuels, coupled with the climate crisis stemming from elevated CO_2 concentrations in the atmosphere, is prompting scientists to pursue the substitution of fossil fuels with renewable and green technologies[1,2]. Ongoing efforts to improve energy storage and conversion systems have led to significant improvements in all components. The cathode electrode in fuel cells and metal-air batteries remains a major bottleneck for carbon-free energy, due to the sluggish kinetics and high overpotentials of the oxygen reduction reaction (ORR)[3,4]. Platinum (Pt) dominates the global ORR market, as this precious metal has the highest catalytic activity in both alkaline and acidic media. Nevertheless, platinum's limited reserves and high-cost result in prohibitively expensive Pt-based cathode electrodes, making large-scale commercialization of fuel cells and metal-air batteries virtually impossible[5]. Furthermore, leaching and agglomeration of Pt nanoparticles lead to a decrease in catalytic activity during operation, limiting the stability of Pt-based electrocatalysts[5,6].

To address this challenge, materials scientists have been actively exploring the development of low-cost electrocatalysts using non-precious metals[7–9]. Electrocatalysts based on non-noble metals have been the subject of extensive research due to their widespread availability and cost-effectiveness in the production of cathode electrodes[10,11]. In this specific context, iron (Fe) is the fourth most abundant element in nature, making Fe_3C nanoparticles a very promising low-cost catalyst for efficiently facilitating the ORR[12–16]. However, the high surface energy of metal nanoparticles makes them thermodynamically unstable under working conditions, resulting in migration, leaching and coalescence during ORR electrocatalysis[17]. These structural modifications often lead to a significant reduction in catalytic performance. Encapsulation of Fe_3C nanoparticles in carbon nanoshells has proved highly effective in protecting metal nanoparticles from catalytic impoverishment over time[18,19].

The exact origin of the ORR activity in carbon nanoshells encapsulating Fe_3C nanoparticles remains unclear. While Fe_3C is not directly exposed to the electrolyte and oxygen molecules, this raises questions about the pathways by which catalytic activity is exerted. One hypothesis suggests that high catalytic performance might involve nitrogen (N) moieties in the carbon nanoshells surrounding the nanoparticles[20], which are often overlooked, but might interact synergistically with Fe_3C to enhance catalytic activity. While some metal nanoparticles are able to promote the catalytic activity of nearby metal active sites via an electronic effect[21–23], the implications of this electronic effect on catalytic enhancement by N species acting as active sites remains unclear. Therefore, controlling N doping in the carbon structure is imperative to understand the additional dynamic mechanisms at play that have not yet been revealed.

In this context, C_1N_1 has emerged as a new two-dimensional (2D) member of the C_xN_y materials, constituting a promising new category of carbon precursors characterized by well-defined textural properties and excellent electrical conductivity[24,25]. C_1N_1 is a porous polymeric carbon precursor with well-defined internal cavities and the ability to interact with transition metals to produce metal nanoclusters after pyrolysis[26]. C_1N_1 is thus anticipated to be an exceptional candidate for producing N-doped carbon shells capable of encapsulating Fe_3C nanoparticles via condensation reactions during carbonization using the internal cavities as nucleation points. Furthermore, the high N doping of the resulting N-doped C_1N_1-derived carbon shell is expected to enhance the interaction between Fe_3C nanoparticles and the carbon substrate, thereby increasing electrical and electrocatalytic properties while preserving most of the shielding properties of graphitic-type core-shell materials.

Inspired by the high catalytic performance of encapsulated Fe_3C nanoparticles and the promising prospects of the new C_1N_1 material, we present the synthesis of a high-performance ORR electrocatalyst derived from C_1N_1. The resultant catalyst comprises N-doped carbon nanoshells encapsulating Fe_3C nanoparticles (NC@Fe_3C-900), demonstrating exceptional activity and superior operational stability in ORR electrocatalysis. The Fe_3C nanoparticle effectively modulates the surface electronic configuration of the thick N-doped carbon nanoshells and enhances the ORR electrocatalytic properties of the N sites in the outermost carbon layer. Moreover, carbon shielded Fe_3C nanoparticles are free from leaching, coalescence and agglomeration of metal nanoparticles, improving ORR electrocatalytic stability. Specifically, NC@Fe_3C-900 exhibits an E_{ONSET} of 0.98 V vs RHE and $E_{1/2}$ of 0.88 V vs RHE, and an improved stability of 97 % after 10,000 s of working time, with a peak power of 0.83 $W \cdot cm^{-2}$ in anion-exchange membrane fuel cells (AEMFC) at 60 ºC. Moreover, density functional theory (DFT) simulations were used to elucidate the fundamental mechanisms governing the observed electrocatalytic enhancements. The computational results provide comprehensive insight into the crucial role played by Fe_3C in enabling significant charge transfer from nanoparticles to the outer carbon layers. This process accounts for the superior electrocatalytic performance at N sites.

Results

The preparation of NC@Fe_3C-900 is illustrated in Figure 1. Briefly, C_1N_1 was synthesized as described in the *Methods* section by carbonizing guanine at 700 ºC under a nitrogen atmosphere. The C_1N_1 model material was characterized by N_2 adsorption-desorption isotherms, which confirmed the presence of well-defined internal cavities ranging from 0.5 to 0.8 nm (Figure S1). Elemental analysis confirmed the ≈ 1:1 C:N ratio (Table S1). The homogeneous distribution of N across the carbon skeleton was checked by STEM images and EDX mapping (Figure S2). The XPS N 1s spectrum of C_1N_1 was also recorded in Figure S3, which was deconvoluted into four peaks [24,27,28]: (i) sp^2 N, typical of triazine and heptazine rings at 398.5 eV, (ii) N in $N\text{-}C_3$ configuration and $-NH_2$ amine-type groups at 399.8 eV, (iii) quaternary N species at 401.2 eV, and (iv) N-O species at 402.9 eV. The significant contribution of the peak at the lowest binding energies aligns with the structure proposed for C_1N_1 compounds. Additional information on the structure and characterization of C_1N_1 can be found in previous studies[24,27,29].

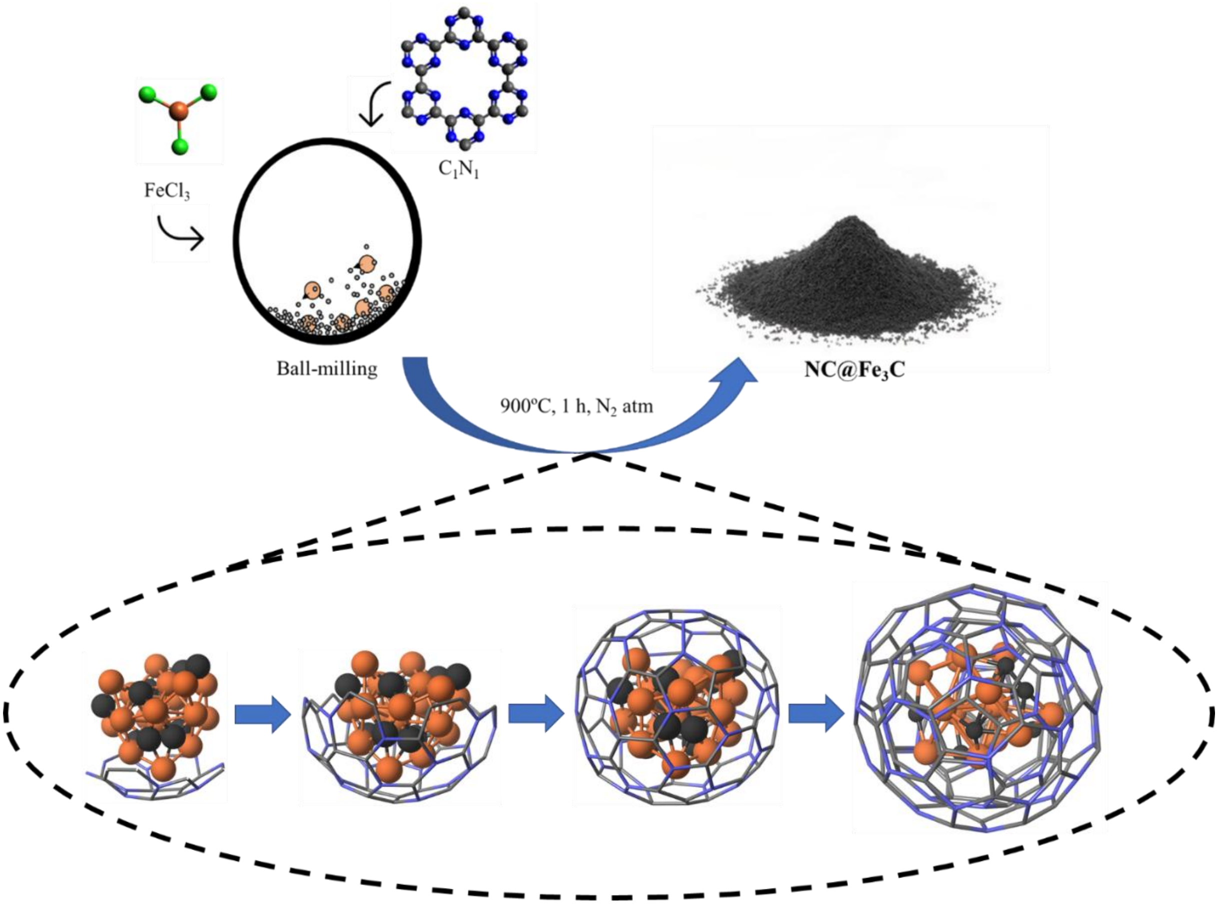

Figure 1: Schematic representation of the encapsulation of Fe_3C nanoparticles by N-doped C_1N_1-derived carbon nanoshells during synthesis. Fe atoms are represented by orange spheres. Carbon atoms in the Fe_3C nanoparticle are represented by black spheres. N-doped C_1N_1-derived carbon encapsulation shells are represented by the stick structure surrounding the Fe_3C core.

Subsequently, Fe was incorporated into the internal cavities of C_1N_1 by mixing the as-prepared C_1N_1 with the Fe precursor in a ball-milling equipment for mechanosynthesis. The resulting mixture underwent heat-treatment at 900 ºC to produce Fe_3C nanoparticles encapsulated in N-doped, C_1N_1-derived carbon shells, called NC@Fe_3C-900. If the pyrolysis temperature is different from 900 ºC, the material is labelled NC@Fe_3C-T, with T representing the heat treatment temperature. HRTEM images confirmed the presence of metallic nanoparticles coated with graphitic-like carbon shells around 20 nm thick in NC@Fe_3C-900 (Figure 2a). The spacing between the carbon layers was 0.370 nm (Figure 2b), which is larger than that of graphite due to the N-doping and other structural defects. The presence of this heteroatom in carbon layers increases the interlayer distance compared relative to purely graphitic materials[30]. The Fast Fourier Transform (FFT) of the carbon nanoshells in Figure 2a exhibits a pattern similar to that of graphitic carbons, confirming the ordered structure around the metallic nanoparticle in NC@Fe_3C. The composition of the nanoparticles was further confirmed by EDX mapping (Figure 2c-e), illustrating a uniform distribution of N and C surrounding the Fe_3C nanoparticles. HRTEM images also revealed graphitic regions devoid of Fe_3C nanoparticles, a consequence of the HCl washing step during the synthesis process (Figure S4). This step effectively removes weakly bound Fe_3C nanoparticles.

The heat-treatment temperature significantly influences the thickness and interlayer spacing of the carbon layers surrounding the Fe_3C nanoparticles (Table S2). As shown in Figure S5, the number of carbon layers surrounding the metal nanoparticles is lower in NC@Fe_3C-700, resulting in an interlayer spacing of 0.385 nm. This indicates a higher degree of N functionalization at lower temperatures. Above 800 ºC, increasing the heat treatment temperature results in thicker carbon nanoshells and lower interlayer spacing (Figure S6 and S7 for NC@Fe_3C-800 and NC@Fe_3C-1000, respectively), signifying a decrease in N content and a better graphitization in the carbon nanoshells at higher temperatures. Nevertheless, it is worth mentioning that the interlayer spacing remains around 0.365 nm in NC@Fe_3C-1000 (Figure S7), which differs from that of undoped graphitic materials and indicates a moderate N content and likely residual structural defects. The Fe content of NC@Fe_3C-900 was estimated to be 14.3 wt.% by Inductively Coupled Plasma – Optical Emission Spectroscopy

(ICP-OES). As shown in Table S1, ICP-OES reveals a low Fe content in NC@Fe_3C-500. The elemental composition in C, N, H and O of all NC@Fe_3C-*T* materials is given in Table S1.

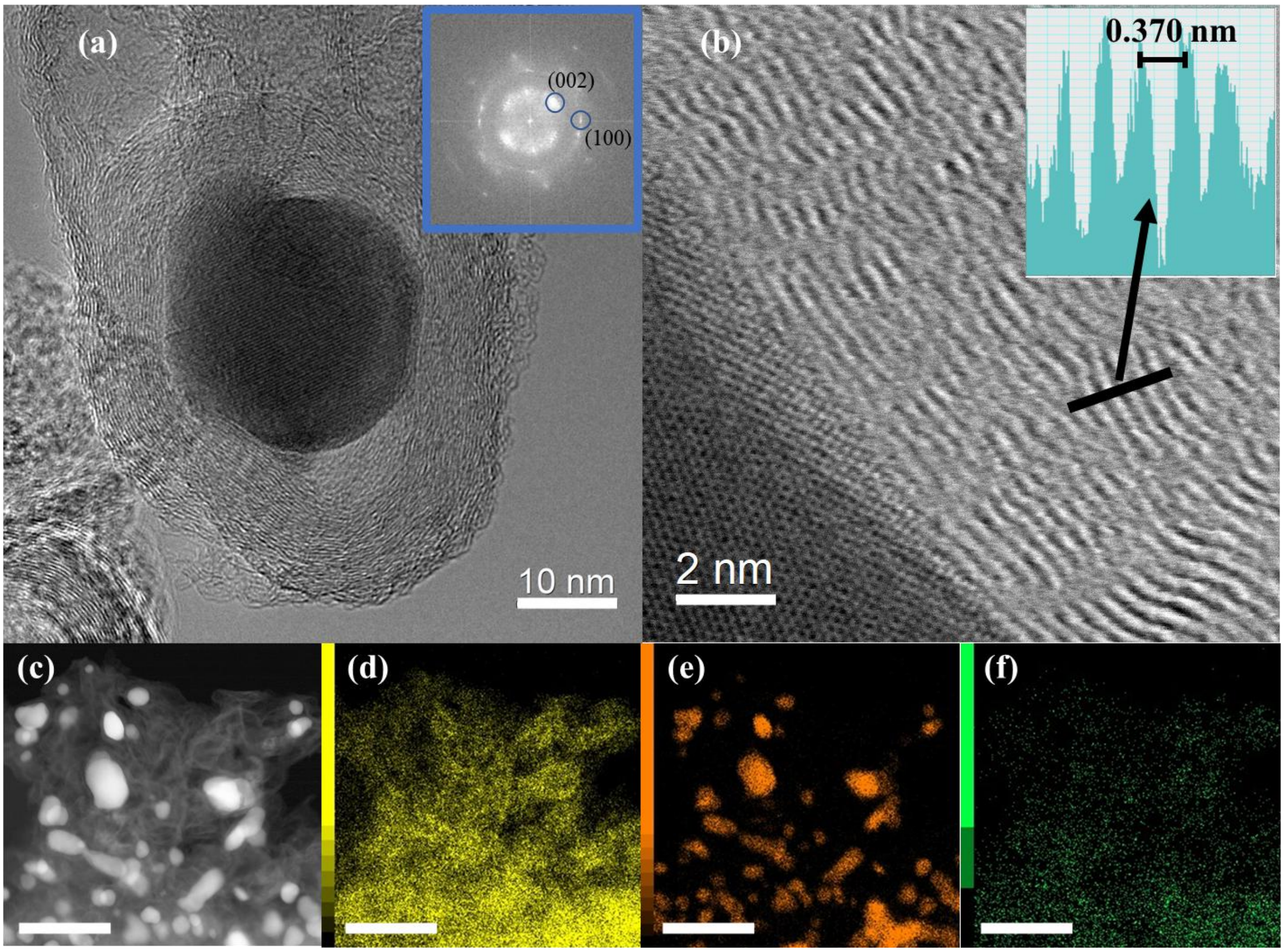

Figure 2: Micrographs. (a) TEM images of NC@Fe_3C-900 material, with a Fe_3C nanoparticle encapsulated in C_1N_1-derived carbon nanoshells (inset: Fast Fourier Transform of the carbon nanoshell phase). (b) High-resolution TEM image (inset: interlayer distance in C_1N_1-derived carbon nanoshell). (c) HAADF-STEM image of NC@Fe_3C-900 material and corresponding EDX mapping of elements (d) C, (e) Fe and (f) N, with scale bars of 200 nm.

The textural properties of the NC@Fe_3C-*T* materials were assessed by N_2 adsorption-desorption isotherms at -196 ºC (Figure 3a), and the data are summarized in Table S3. As observed in Figure 3a, the introduction of Fe_3C nanoparticles in N-doped, C_1N_1-derived carbon shells results in no significant change in the textural properties of NC@Fe_3C-900 relative to pristine C_1N_1 (see again Figure S1). Minor differences are noticeable in the NC@Fe_3C-500 and NC@Fe_3C-700 materials (Figure S8). However, the surface area (S_{2D-}

$_{NLDFT}$) of pristine C_1N_1, initially 280 m^2 g^{-1}, increases to 310 - 330 m^2 g^{-1} with similar adsorption profiles for a heat treatment temperature of 800 ºC or higher, revealing no substantial differences in textural properties. The pore size distribution (PSD) and the cumulative pore volume of NC@Fe_3C-900 (Figure S9) confirm a hierarchical structure with the presence of the same internal cavities at 0.5 and 0.8 nm as those observed for pristine C_1N_1, as well as the presence of micro- and mesopores. Figures S10 and S11 show the PSDs and cumulative pore volumes for all other NC@Fe_3C-*T* materials.

The crystal structure of NC@Fe_3C-900 was further examined by X-ray diffraction (XRD). As observed in Figures 3b, NC@Fe_3C-900 exhibits a peak around 26º, which corresponds to the (002) band of graphitic carbon (PDF 41-1487). Higher heat treatment temperatures lead to a narrower (002) band, indicating an increasing degree of graphitization. Samples obtained at temperatures below 700 ºC does not reveal the presence of iron carbide (see Figure S12). This observation suggests that Fe_3C formation occurs at temperatures of around 800 ºC (Figure S13) along with graphitization of the carbon layers encapsulating the metallic Fe_3C nanoparticles. Metallic phases were not detected in NC@Fe_3C-500 either (Figure S14).

Raman spectroscopy was used to better understand the structural order and graphitization degree of NC@Fe_3C-*T* materials. The Raman spectrum of NC@Fe_3C-900 (Figure 3c) displays the D and G bands characteristic of carbon-based materials at 1330 and 1580 cm^{-1}, respectively associated with the vibrational modes of disordered carbon and graphitic regions. NC@Fe_3C-900 shows an I_D/I_G ratio of 1.0, which is similar to analogous NC@Fe_3C-*T* materials produced at different temperatures (I_D/I_G ratio ranging from 1.0 to 1.1, see Figure S15)[31,32]. The 2D Raman band, approximately at 2685 cm^{-1} and associated with crystalline graphene, is distinctly present in NC@Fe_3C-*T* materials obtained at 800 ºC and above. In the second-order part of the Raman spectra, the peak associated with the D + D' band was also found at around 2900 cm^{-1} for temperatures above 800 ºC. The D + D' band arises from the combination of phonons with different momenta, which is strongly associated with the presence of defects or doping in the graphitic layers[33,34]. Recognized as a catalyst for graphitization, Fe promotes in-situ graphitization of neighboring carbonaceous regions at elevated temperatures[35]. Consequently, this process leads to the formation of N-doped graphite-like nanoshells encapsulating Fe_3C nanoparticles, as observed in HRTEM images (see again Figure 1). NC@Fe_3C-*T* materials obtained at temperatures lower than 700 ºC (Figure S15) show a broad contribution around 3000 cm^{-1}, associated with a second-order peak originating from the D-G combination in C_1N_1[24,36]. On the other hand, NC@Fe_3C-500 and NC@Fe_3C-700 show a small contribution around 600-800 and 1000 cm^{-1}, typically assigned to the vibrational modes of pyrazine and triazine rings present in pristine C_1N_1[24,36].

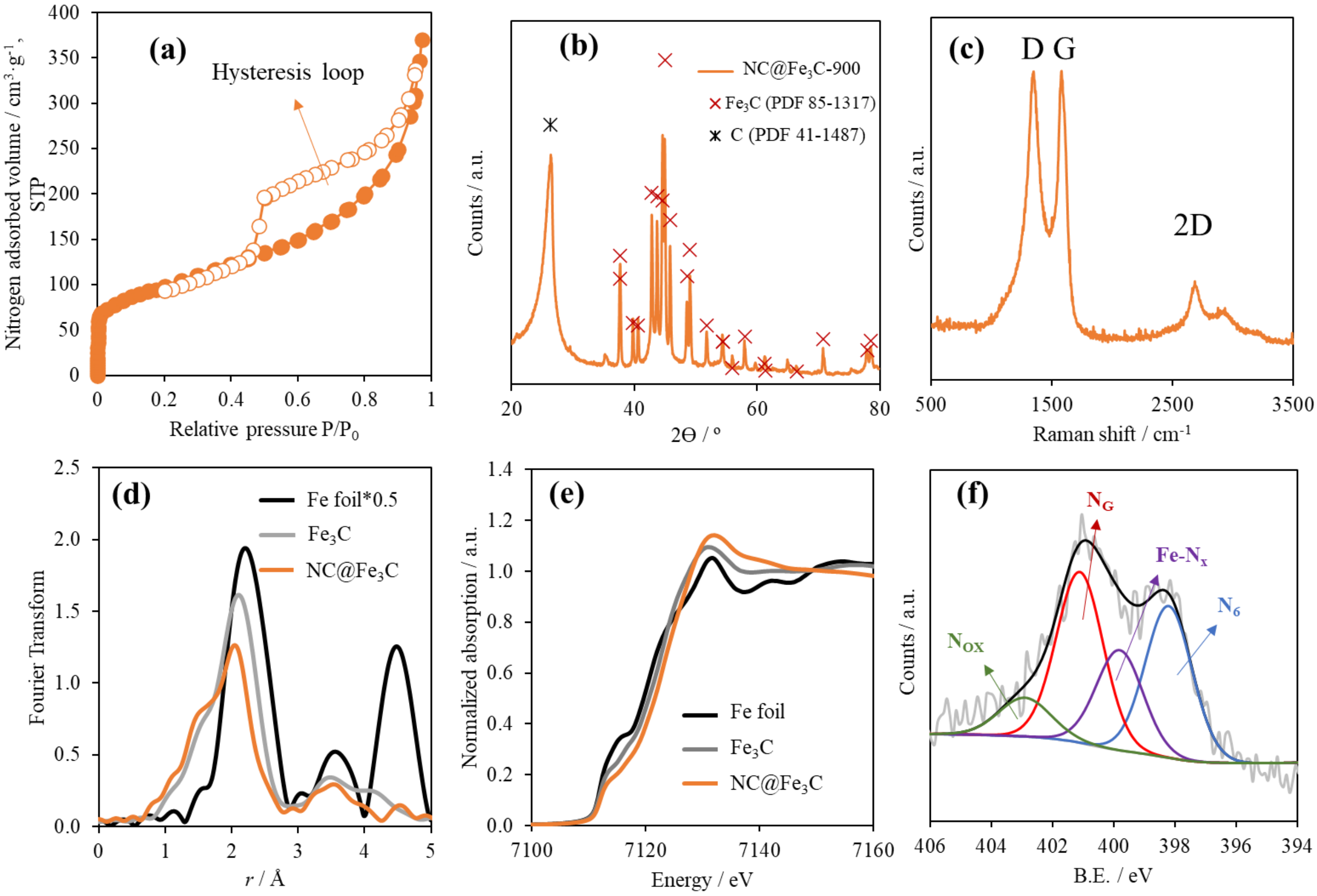

Figure 3: Physicochemical characterization of NC@Fe_3C-900. (a) N_2 adsorption-desorption isotherm at -196 ºC. (b) XRD pattern. (c) Raman spectrum at 532 nm. (d) Non-phase-shift corrected FT-EXAFS profiles of NC@Fe_3C-900, Fe metal foil and Fe_3C as references, and (e) comparison between experimental Fe K-edge XANES spectra of NC@Fe_3C-900, Fe metal foil and Fe_3C as references. (f) XPS N 1s spectrum; the blue peak

represents pyridinic N (N_6), the violet peak represents Fe-N groups (Fe-N_x), the red peak represents graphitic N (N_G), and the green peak represents N-O species (N_{OX}).

X-ray absorption spectroscopy (XAS) was performed to precisely examine the nature and local structure of Fe species in NC@Fe_3C-900. Figure 3d shows the Fourier Transform (FT) of the extended X-ray absorption fine structure (EXAFS) spectrum, which reveals a prominent peak around 2 Å. This peak is assigned to Fe-Fe backscattering from Fe_3C and closely matches that of the reference compound Fe_3C. It is worth mentioning that XAS experiments failed to detect the presence of Fe in the form of single atoms, with only Fe_3C detected, in agreement with HRTEM images. Examination of the Fe K-edge X-ray absorption near edge structure (XANES) spectrum of NC@Fe_3C-900 in Figure 3e shows a notable positive shift in the absorption threshold relative to the Fe_3C reference spectrum. This shift corresponds to the presence of a fraction of Fe in a higher oxidation state.

X-Ray photoelectron spectroscopy (XPS) was used to further characterize the surface chemistry and electronic structure of NC@Fe_3C-*T* materials. Table S4 summarizes the surface chemical composition of all materials. XPS quantification consistently shows low Fe content in the surface chemistry of all NC@Fe_3C-*T* materials, indicating robust encapsulation of Fe_3C nanoparticles. In the high-resolution Fe 2p spectrum, traces of Fe are detected in the surface chemistry of NC@Fe_3C-900. The signal of zero-valent Fe, which is often attributed to Fe_3C, is vaguely detected, indicating encapsulation of Fe_3C nanoparticles (Table S4)[37,38]. Nevertheless, a slight contribution of Fe species in a higher oxidation state is observed at 710.4 - 710.8 eV in all NC@Fe_3C-*T* materials (Figure S16).[29,30] At 700 ºC, the zero-valent Fe peak is slightly observed, as Fe_3C nanoparticles are less encapsulated at these temperatures. As previously shown in HRTEM images, temperatures above 800 ºC are required to promote the formation of thick N-doped carbon nanoshells.

The XPS N 1s spectrum (Figure 3f) reveals the presence of four main species[39–41]: pyridinic N at 398.2 eV, Fe-N at 399.7 eV, graphitic N at 401.2 eV, and N-O-type species at 402.9 eV.

The high pyridinic and graphitic N content is beneficial for the ORR as it enhances the local electronic conductivity in carbon materials, further improving the electron transfer properties in the presence of Fe-N species[42]. As observed in Table S4, the graphitic N content increases with the temperature of the heat treatment, which means that greater electronic transfer is expected in the carbon layers of materials obtained at higher temperatures. The C 1s spectra of NC@Fe_3C-*T* materials were deconvoluted into three peaks located at 284.6, 285.3 and 286.4 eV, which are related to C=C, C=N/C=O and C-O, respectively (Figure S18). C 1s, N 1s and O 1s spectra of the NC@Fe_3C-T materials are included in Figure S17, S18 and S19, respectively. As observed, the higher the heat treatment temperature, the greater the contributions of C=C and graphitic N, indicating a higher graphitization degree in the samples obtained at higher temperatures.

The electrocatalytic ORR activity of NC@Fe_3C-900 was evaluated in an O_2-saturated 0.1 M KOH solution by linear sweep voltammetry (LSV) in a three-electrode cell with a rotating ring-disk electrode (RRDE). All other NC@Fe_3C-*T* materials and commercial Pt/C were also evaluated for comparison. As shown in Figure 4a, the NC@Fe_3C-900 material exhibited exceptional catalytic performance, with an outstanding onset potential (E_{ONSET}) of 0.98 V and a half-wave potential ($E_{1/2}$) of 0.88 V vs RHE. Notably, these values surpassed the ORR catalytic performance of commercial Pt/C electrocatalysts (E_{ONSET} = 0.96 V and $E_{1/2}$ = 0.84 V vs RHE).

Excellent catalytic activities were also recorded in both NC@Fe_3C-800 and NC@Fe_3C-1000 samples, with E_{ONSET} of 0.94 V and $E_{1/2}$ of 0.84 V vs RHE, similar to that of commercial Pt/C electrocatalysts, followed by NC@Fe_3C-700 with an E_{ONSET} of 0.91 V vs RHE (Figure S20). The similar surface chemistry and encapsulation thickness of Fe_3C in NC@Fe_3C-800 and NC@Fe_3C-1000 also lead to high catalytic performance, while the low Fe_3C content and the lack of a thick encapsulation in NC@Fe_3C-700 justify its comparatively lower catalytic performance. At 500 ºC, the catalytic activity of the materials aligns with that of pristine C_1N_1

material. This similarity is attributed to the low carbonization temperatures, which do not sufficiently promote a strong interaction between Fe atoms and the N-doped C_1N_1-derived carbon material. As a consequence, Fe atoms are weakly bound to the carbon and subsequently removed during the washing step of the synthesis procedure. This conclusion is confirmed by ICP-OES analysis (see Table S1). The performance of NC@Fe_3C-900 surpasses that of Pt/C, although the Fe_3C nanoparticles are encapsulated in 30 carbon layers, which completely rules out the possibility of a direct action of the Fe_3C nanoparticles as active sites. Instead, it is likely that the N species present in the outer layers of the carbon nanoshells are responsible for the enhanced catalytic activity. However, the catalytic activity of NC@Fe_3C-900 far exceeds that of N-doped metal-free carbon materials[43], suggesting that Fe_3C nanoparticles activate or enhance the ORR activity of N species located in the outer carbon layers of the encapsulation.

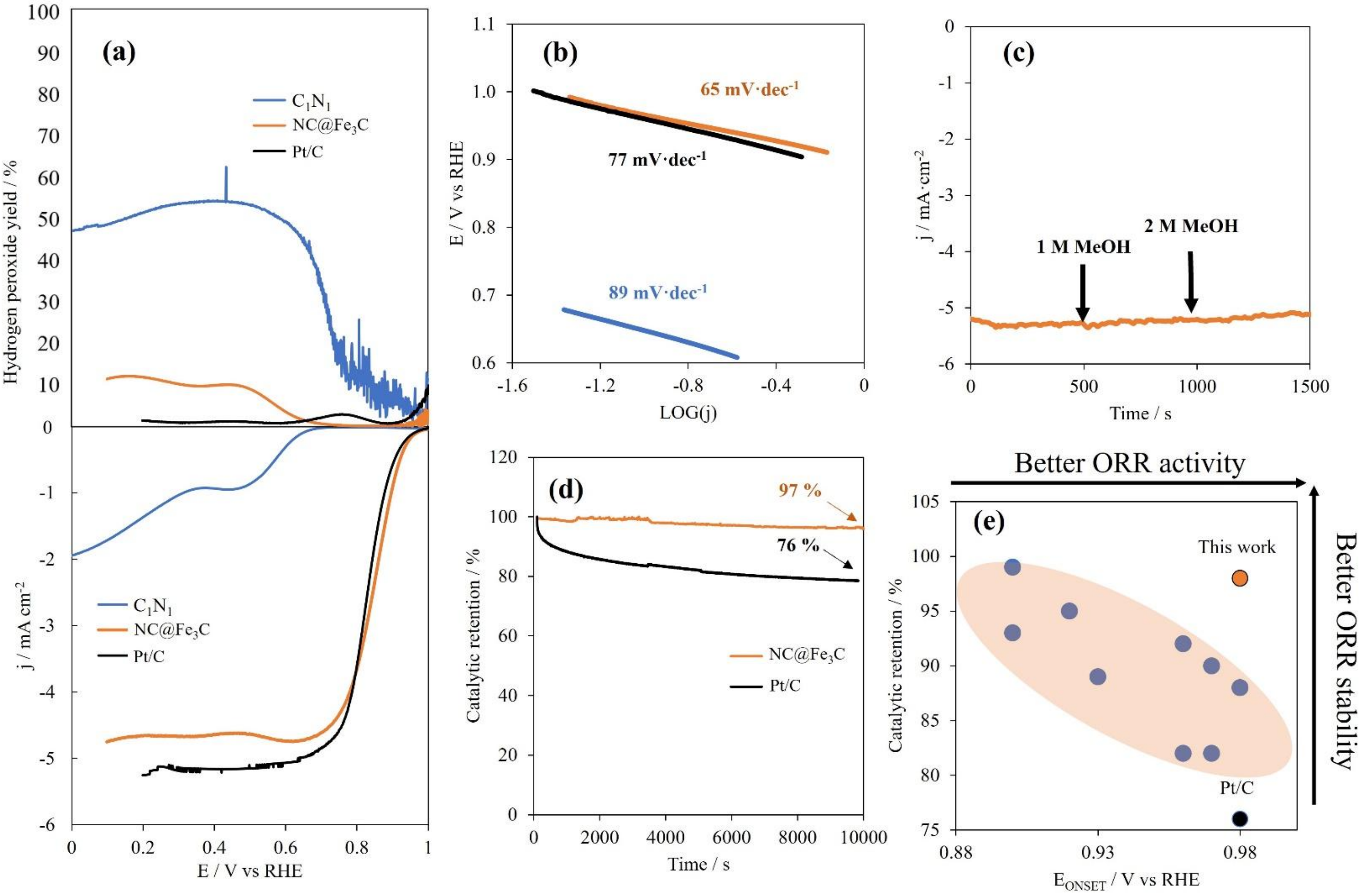

Figure 4: Electrocatalytic performance of NC@Fe_3C-900 for the ORR. (a) Hydrogen peroxide yield and LSV curves of pristine C_1N_1, NC@Fe_3C-900 and commercial Pt/C electrocatalysts in an O_2-saturated 0.1 M KOH solution at 5 mV·s^{-1} and 1600 rpm. (b) Tafel plots of pristine C_1N_1, NC@Fe_3C-900 and commercial Pt/C electrocatalysts obtained from LSV curves. (c) MeOH tolerance test of NC@Fe_3C-900. (d) Chronoamperometric response of NC@Fe_3C-900 and Pt/C in an O_2-saturated 0.1 M KOH solution. (e) Comparison of ORR electrocatalytic activity and durability of NC@Fe_3C-900 with other Fe-N-C catalysts available in the open literature. The black diamond represents Pt/C electrocatalysts, the blue disks represent Fe-N-C catalysts reported in the open literature, and the orange triangle represents NC@Fe_3C-900.

The ORR mechanisms were further evaluated by determining the hydrogen peroxide yield, calculated from the current density of the platinum ring during RRDE measurements. Notably, in the operational potential range suitable for fuel cells (i.e., from 0.6 V to E_{ONSET}), the H_2O_2 yield approaches 0 %, displaying values similar to those of Pt/C electrocatalysts. However, the NC@Fe_3C-700 material exhibits a substantial increase in H_2O_2 yield, attributed to the presence of different metal phases and the poor encapsulation effect. Lower Tafel slopes (Figure 4b) were obtained for NC@Fe_3C-900 (65 mV dec^{-1}) compared to commercial Pt/C (77 mV dec^{-1}), which reveals different rate-determining steps and, therefore, ORR mechanisms. A methanol tolerance test was carried out to evaluate the resistance of NC@Fe_3C-900 to poisoning. As observed in Figure 4c, the catalytic activity of NC@Fe_3C-900 remained unchanged after the addition of methanol at concentrations of 1.0 and 2.0 M.

The activity stability of NC@Fe_3C-*T* materials was assessed by chronoamperometric measurements in an O_2-saturated 0.1 M KOH solution at fixed potential (Figure S21). As observed in Figure 4d, NC@Fe_3C-900 as the cathode electrode demonstrates high activity retention, maintaining 97 % catalytic activity after 10,000 s, compared to Pt/C, which achieves only 76 % under the same conditions and for the same duration. The N-doped carbon nanoshells derived from C_1N_1 not only enhance electron transfer more effectively than ordinary carbon shells but also serve as a robust shield, preventing leaching, coalescence and agglomeration of Fe_3C nanoparticles. This shielding effect maintains catalytic activity over extended working periods. The assessment of the catalytic stability of NC@Fe_3C-*T* materials highlights the shielding effect of carbon. Materials obtained at temperatures of 800 ºC and above exhibit superior operational durability ranging from 96 to 98 % (Figure S22), while those obtained at 700 ºC or below show lower catalytic retention. The lower Fe_3C content and the tighter encapsulation observed in NC@Fe_3C-700 lead to greater exposure of the nanoparticles, making them more susceptible to lixiviation and dissolution in the electrolyte. As shown in Figure 4e, an extensive literature review was carried out to compare the catalytic activity and operational durability of NC@Fe_3C-900 with the most recent findings in this field. Figure 4e shows the catalytic activity (E_{ONSET}) as a function of catalytic retention for state-of-the-art Fe-based electrocatalysts. It is evident that NC@Fe_3C-900 exhibits superior operational stability under working conditions compared with any other Fe-based electrocatalysts, while demonstrating ORR catalytic activity similar to that of platinum.

The catalytic activity of NC@Fe_3C-900 in the ORR under acidic conditions was evaluated using an O_2-saturated 0.5 M H_2SO_4 solution. Figure S23 shows the LSV curves of NC@Fe_3C-*T* materials, demonstrating excellent catalytic activity. The sample synthesized at 1000 ºC showed the highest performance, exhibiting an E_{ONSET} of 0.83 V vs RHE, closely followed by those obtained at 800 and 900 ºC. This E_{ONSET} value exceeds most Fe-based electrocatalysts in the literature using an acid electrolyte. Conversely, NC@Fe_3C-700 demonstrated a significant reduction in both limiting current density and E_{ONSET} (0.65 V vs RHE). Furthermore, NC@Fe_3C-500 showed no discernible catalytic activity over the recorded potential range (not included for the sake of clarity). High-temperature treatment is thus mandatory to produce Fe_3C nanoparticles embedded in N-doped C_1N_1-derived carbon nanoshells with high graphitic N content, which enhances the catalytic activity of the materials. The H_2O_2 yield was also evaluated to determine the selectivity of the reaction. Irrespective of the heat treatment temperature, NC@Fe_3C-*T* materials at temperatures above 800 ºC show a negligible H_2O_2 formation and, thus, a 4-electron pathway across the entire potential range. This demonstrates the high selectivity towards water formation in acidic solution.

In addition, the catalytic stability of NC@Fe_3C-*T* materials in acidic medium was evaluated by chronoamperometric measurements in an O_2-saturated 0.5 M H_2SO_4 solution. As observed in Figure S24, the catalytic retention values were lower than those obtained in alkaline medium. Nevertheless, a noticeable difference persisted in catalytic retention as a function of encapsulation thickness. NC@Fe_3C-*T* materials characterized by thicker encapsulation indeed showed enhanced catalytic retention, reaching 82 % in NC@Fe_3C-1000 after 10,000 s. In contrast, materials obtained at 800 and 900 ºC showed a drop in catalytic retention, falling to 66 and 71 %, respectively. The absence of encapsulation in NC@Fe_3C-700 results in a substantial decrease in catalytic activity over time, reaching only 30% of catalytic activity after the same duration. It is well established that the catalytic stability of Fe-based electrocatalysts tends to be lower in acid electrolytes than in alkaline media. However, the performance of NC@Fe_3C-*T* materials underlines the key role that N-doped C_1N_1-derived carbon shells might play in enhancing both the catalytic activity and stability of Fe_3C nanoparticles during ORR in acidic media.

The in-situ electrocatalytic activity of NC@Fe_3C-900 in anion-exchange membrane fuel cells (AEMFC) was evaluated using polarization and power density curves. As observed in Figure 5a, the AEMFC equipped with the NC@Fe_3C-900 cathode exhibits state-of-the-art catalytic performance, with a peak power density of 830 $mW \cdot cm^{-2}$ achieved even at the relatively low operating temperature of 60 °C. This performance agrees with the kinetic results obtained from the RRDE measurements. However, in the AEMFC setup, the catalyst showed a mass activity of 200 $A \cdot g^{-1}$. This value exceeds the observation in RRDE, calculated from LSV curves at 0.8 V vs RHE (5 $A \cdot g^{-1}$), attributed to variations related to environmental differences between AEMFC (i.e., 60 °C and O_2 in gas phase) and RRDE (i.e., 25 ºC in an O_2-saturated

0.1 M KOH solution), including differences in temperature and oxygen phase. In a comparative evaluation with Fe-based electrocatalysts under similar conditions (i.e., a temperature around 60 ºC and catalysts loading of around 1 mg·cm^{-2}) reported in the literature [44–58], the catalytic performance of the NC@Fe_3C-900 cathode in this study demonstrates notably superior power density values, as shown in Figure 5b, surpassing those extensively reported in the literature.

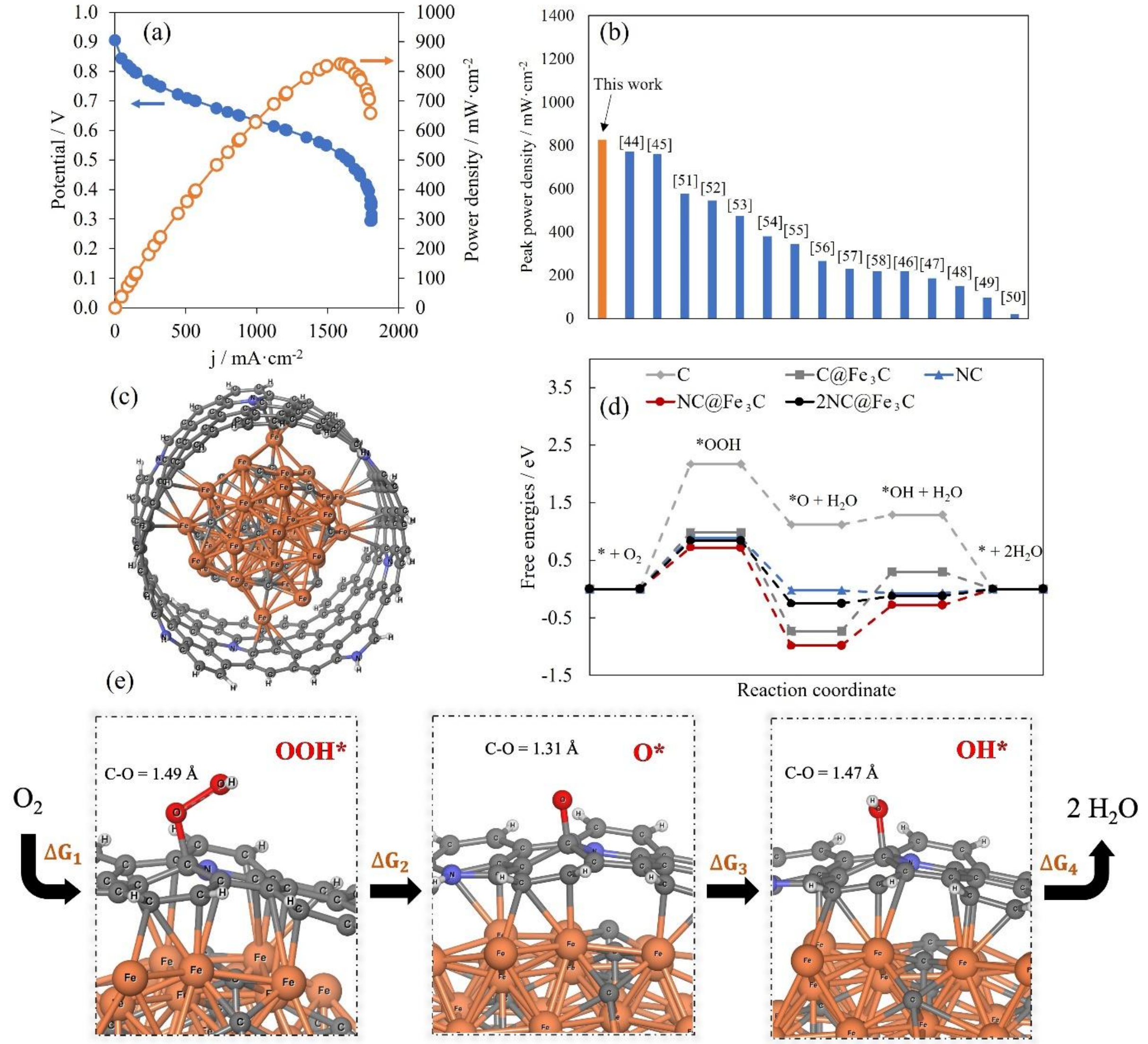

Figure 5: Electrochemical test of NC@Fe_3C-900 in AEMFC, and DFT simulations. (a) Curves of H_2/O_2 AEMFC potential vs. current density (solid blue) and power density vs. current density (dashed orange) for the NC@Fe_3C-900 cathode at 60 ºC under H_2/O_2 flows of 1 L·min^{-1}. The anode consisted of 0.6 mg·cm^{-2} of 60 wt.% PtRu/C. (b) Comparison of the AEMFC peak power density of NC@Fe_3C-900 with other Fe-N-C catalysts available in the open literature. (c) Illustration of the NC@Fe_3C model material, with hydrogen (H) shown in white, carbon (C) in brown, nitrogen (N) in grey, and iron (Fe) in yellow. (d) ORR free energy diagrams shown

for all model systems (see text) at a potential of U = 1.23 V vs. RHE. (e) Illustration of all ORR intermediates when using the NC@Fe_3C model system.

In order to elucidate the underlying mechanisms behind the remarkable catalytic activity of NC@Fe_3C-900, which is the best electrocatalyst, although not the one with the most carbon layers, we carried out density functional theory (DFT) simulations. Our study involved the analysis of five distinct model systems called C, NC, C@Fe_3C, NC@Fe_3C and 2NC@Fe_3C, as detailed in the structural model section. This comprehensive examination allows us to better understand the complex interaction between Fe_3C nanoparticles and N-doped carbon layers. It should be pointed out here that the modeling of 2 carbon layers alone, although carried out with significant computing resources (i.e., those of a university computing mesocenter), has already cost more than a month of computing time, and that the simulation of several dozen carbon layers under these conditions was totally out of reach.

Figure 5c thus illustrates the NC@Fe_3C model system, while Figure 5d shows the ORR free energy diagram for all model electrocatalysts at the thermodynamic potential (U = 1.23 V). The free energy variations and Gibbs free energies are gathered in Table S5 and S6, respectively, and the ORR intermediates are illustrated in Figure 5e, S25 and S26. The evolution of the electron densities and charges of the C, NC and 2NC systems is also presented in Figure S28 and Table S7, respectively. Our computational results reveal that both carbon (C) and N-doped carbon (NC) model systems exhibit low ORR catalytic activity, showing high predicted ORR overpotentials and the rate-determining step (RDS) in the first reduction (*OOH) (Table S5). The low activity of the C system can be explained by the absence of charge transfer upon adsorption (*OOH), as highlighted in Figure S28 and Table S7, and by the very high charge transfer required to reach the *O step (up to 0.8 e from the carbon layer to the O atom). In contrast, the incorporation of Fe_3C cores into the carbon layer significantly activates the carbon surface towards the ORR by reducing thermodynamic barriers and stabilizing the *O intermediate (Table S6). Furthermore, the NC and 2NC systems chemically activate the*OOH species, as a significant charge transfer is observed. Moreover, by incorporating the Fe_3C core into these systems, two RDS are observed in the reaction mechanism (*OOH and *OH), implying two limiting steps in the ORR (Table S5). An in-depth analysis of the Bader charge reveals a clear correlation between electron transfer and the presence of Fe_3C core and N doping (Figures S27, S28 and Table S7). While Fe_3C alone does not provide sufficient electron transfer to the carbon layer (C@Fe_3C system), the incorporation of N atoms into the C layers (NC@Fe_3C) markedly enhances electron transfer from the Fe_3C core (Figure S27), which effectively stabilizes the *O intermediate by occupying the vacant "*sp*" states. The positive Bader charge of the Fe_3C core in the ORR intermediates of the NC@Fe_3C system reveals that N doping facilitates electron delivery from Fe_3C nanoparticles to the active sites of the carbon layers (Table S7).

The introduction of two carbon layers (2NC@Fe_3C) leads to a slight increase in the first RDS of the 2NC@Fe_3C system (Table S5), manifested by a 0.12 V increase in the theoretical overpotential (Table S6). This suggests a limited impact of additional carbon layers on the influence exerted by Fe_3C. This result aligns with previous theoretical research, indicating that the impact of the Fe_3C nanoparticle on the outermost carbon shell decreases as the number of carbon layers increases[59,60]. However, it is also observed that the energy associated with the second RDS (formation of the *OH intermediate) practically disappears when a second layer of N-doped carbon is included. This reduction correlates with the slight decrease in binding strength of the *O intermediate in 2NC@Fe_3C. This indicates that, although the first RDS has slightly increased in thermodynamic terms (+0.12 eV), the second RDS has been significantly reduced in the 2NC@Fe_3C system (-0.57 eV), which suggests an increase in the ORR catalytic activity in multilayer systems. Moreover, Bader charge calculations (see Table S7) demonstrate that there is still electron transfer from the Fe_3C core to the active sites located in the second carbon layer. Therefore, the outstanding catalytic activity observed experimentally in the NC@Fe_3C-900 is the consequence of optimal parameters. The fact that NC@Fe_3C-900 is an optimum material could be due to better protection of the Fe_3C by a sufficient thickness of carbon layers and by crystallized Fe_3C of better quality or in greater proportion, which materials prepared at lower temperatures cannot achieve. At the same time, if the processing temperature is too high (1000 °C), the amount of nitrogen doping of the carbon layers decreases and the catalyst becomes less and less effective. In support of this argument, numerous studies on Fe-C-N electrocatalysts have shown that it is necessary to have all three elements together, and that if N is missing, it works much less well[61,62]. Nor can it be ruled out that Fe_3C treated at too high temperature, and although already properly crystallized, starts to lose its catalytic properties due to the presence of fewer and fewer intrinsic defects, which are always useful in this kind of reaction.

In the end, the 30 carbon layers of NC@Fe_3C-900 provide a sufficient protective effect to enable excellent in operando stability, whereas the high N doping, especially through graphitic nitrogen species, promotes enhanced electronic conductivity. This allows excellent electron transfer from the Fe_3C core to the active N sites in the outermost carbon layer[63]. Fueled by the electron transfer from Fe_3C nanoparticles, these active N sites exhibit higher catalytic activity than metal-free N-doped carbon materials, enabling state-of-the-art electrocatalytic performance.

Conclusions

Fe_3C nanoparticles were systematically encapsulated in N-doped C_1N_1-derived carbon nanoshells using a two-step approach. XAS and STEM experiments confirmed the Fe_3C nature of the nanoparticles and the successful encapsulation in N-doped graphitic-type layers. The catalytic activity of NC@Fe_3C-900 exceeded that of commercial Pt/C electrocatalysts, showing no degradation even after 10,000 s of operation. AEMFC measurements demonstrated state-of-the-art performance in fuel cell experiments with a peak power density of 830 mW·cm^{-2}. Additionally, the thick encapsulation acts as a protective carbon shield, preserving catalytic activity over time. Therefore, NC@Fe_3C-900 acts as a robust and highly active Fe-N-C catalyst, offering a promising alternative to Pt/C in AEMFCs. DFT simulations have revealed essential information about the mechanism involving electron transfer from Fe_3C to the outer carbon layers. This phenomenon enhances the kinetics of oxygen reduction at the N sites of the outermost layers. These findings mark a significant advance in fundamental chemistry, with potential implications for fuel cell technology.

Acknowledgements

All authors thank the "Microscopies, Microprobes and Metallography (CC3M)" platform at the Institut Jean Lamour (Nancy, France) for granting access to TEM facilities. Our special thank go to Prof. Paul Kohl at Georgia Tech, who supplied us with the polymer materials used to manufacture AEMFCs. The modeling contribution was granted access to the HPC resources of TGCC under the allocation 2023-A0140810433 made by GENCI.

Funding

We have received funding from the French PIA project “Lorraine Université d’Excellence”, reference ANR-15-IDEX-04-LUE, and from the ERDF-funded TALiSMAN and TALiSMAN2 projects. SGD thanks the Ministerio de Universidades, the European Union and the University of Oviedo for their financial support (MU-21-UP2021-030 30267158).

Authors’ contributions

J.Q.B and S.G.D. designed the NC@Fe_3C materials and carried out the synthesis. M.E. carried out the microscopy experiments. M.T.I. performed the XPS analysis. A.D. and M.B. performed DFT calculations. J.Q.B and S.G.D. performed the electrocatalytic measurements. Y.C. and W.M. performed the AEMFC experiments. J.C.G. conducted the adsorption isotherm studies. A.Z. performed the XAS measurements. A.C carried out Raman studies. J.Q.B, A.C. and V.F. conceived the project and wrote this manuscript. All the authors participated in the discussion of the results.

Competing interests

The authors declare no competing interests.

References

(1) Parimala, P. V. S. S. A.; Sharma, D.; Mathew, R. A Comprehensive Review on the Advances in Renewable Wind Power Technology. *Wind Engineering* **2023**, *47*, 442–463.

(2) Khan, T.; Yu, M.; Waseem, M. Review on Recent Optimization Strategies for Hybrid Renewable Energy System with Hydrogen Technologies: State of the Art, Trends and Future Directions. *Int J Hydrogen Energy* **2022**, *47*, 25155–25201.

(3) Dessalle, A.; Quílez-Bermejo, J.; Fierro, V.; Xu, F.; Celzard, A. Recent Progress in the Development of Efficient Biomass-Based ORR Electrocatalysts. *Carbon* **2023**, *203*, 237–260.

(4) Quílez-Bermejo, J.; Morallón, E.; Cazorla-Amorós, D. Metal-Free Heteroatom-Doped Carbon-Based Catalysts for ORR. A Critical Assessment about the Role of Heteroatoms. *Carbon* **2020**, *165*, 434–454. https://doi.org/10.1016/j.carbon.2020.04.068.

(5) Morozan, A.; Jousselme, B.; Palacín, S. Low-Platinum and Platinum-Free Catalysts for the Oxygen Reduction Reaction at Fuel Cell Cathodes. *Energy Environ Sci* **2011**, *4*, 1238–1254.

(6) Stacy, J.; Regmi, Y. N.; Leonard, B.; Fan, M. The Recent Progress and Future of Oxygen Reduction Reaction Catalysis: A Review. *Renewable and Sustainable Energy Reviews* **2017**, *69*, 401–414.

(7) Yang, Z.; Chen, Y.; Zhang, S.; Zhang, J. Identification and Understanding of Active Sites of Non-Noble Iron-Nitrogen-Carbon Catalysts for Oxygen Reduction Electrocatalysis. *Adv Funct Mater* **2023**, 2215185.

(8) Das, C.; Subgam, B.; Roy, P. Transition Metal Non-Oxides as Electrocatalysts: Advantages and Challenges. *Small* **2022**, *18*, 2202033.

(9) Chen, Q.; Zhang, Z.; Zhang, R.; Hu, M.; Shi, L.; Yao, Z. Recent Progress of Non-Pt Catalysts for Oxygen Reduction Reaction in Fuel Cells. *Processes* **2023**, *11*, 361.

(10) Wang, D.; Pan, X.; Yang, P.; Li, R.; Xu, H.; Li, Y.; Meng, F.; Zhang, J.; An, M. Transition Metal and Nitrogen Co-Doped Carbon-Based Electrocatalysts for the Oxygen Reduction Reaction: From Active Site Insights to the Rational Design of Precursors and Structures. *ChemSusChem* **2021**, *14*, 33–55.

(11) Niu, W. J.; He, J. H.; Gu, B. N.; Liu, M. C.; Chueh, Y. L. Opportunities and Challenges in Precise Synthesis of Transition Metal Single-Atom Supported by 2D Materials as Catalysts toward Oxygen Reduction Reaction. *Adv Funct Mater* **2021**, *31*, 2103558.

(12) Martinez, U.; Komini-Babu, S.; Holby, E. F.; Chung, H. T.; Yin, X.; Zelenay, P. Progress in the Development of Fe-Based PGM-Free Electrocatalysts for the Oxygen Reduction Reaction. *Advanced Materials* **2019**, *31*, 1806545.

(13) Wan, X.; Chen, W.; Yang, J.; Liu, M.; Liu, X.; Shu, J. Synthesis and Active Site Identification of Fe−N−C Single-Atom Catalysts for the Oxygen Reduction Reaction. *ChemElectroChem* **2019**, *6*, 304–315.

(14) Shen, H.; Thomas, T.; Rasaki, S. A.; Saad, A.; Hu, C.; Wang, J.; Yang, M. Oxygen Reduction Reactions of Fe-N-C Catalysts: Current Status and the Way Forward. *Electrochemical Energy Reviews* **2019**, *2*, 252–276.

(15) Wu, G.; Shao, C.; Cui, B.; Chu, H.; Qiu, S.; Zou, Y.; Xu, F.; Sun, L. Honeycomb-like Fe/Fe3C-Doped Porous Carbon with More Fe–Nx Active Sites for Promoting the Electrocatalytic Activity of Oxygen Reduction. *Sustain Energy Fuels* **2021**, *5*, 5295–5304.

(16) Xie, T.; Hu, J.; Xu, Q.; Zhou, C. Metal-Organic Framework Derived Fe3C Nanoparticles Coupled Single-Atomic Iron for Boosting Oxygen Reduction Reaction. *J Colloid Interface Sci* **2023**, *630*, 688–697.

(17) Gao, C.; Lyu, F.; Yin, Y. Encapsulated Metal Nanoparticles for Catalysis. *Chem Rev* **2021**, *121*, 834–881.

(18) Yu, H.; Liu, D.; Srinivas, K.; Ma, F.; Zhang, Z.; Wang, M.; Wu, Y.; Wang, Y.; Li, X.; Chen, Y. Core-Shell Fe/Fe3C Heterostructure@carbon Layers Anchored on N-Doped Porous Carbon for Boosting Oxygen Reduction Reaction. *J Alloys Compd* **2023**, *949*, 169863.

(19) Yuan, Y.; Liu, Y.; Li, C.; Feng, S.; Liu, Q.; Huo, J. Hierarchically Porous N-Doped Carbon Nanosheet Networks with Ultrafine Encapsulated Fe3C and Fe-Nx for Oxygen Reduction Reaction in Alkaline and Acidic Media. *J Alloys Compd* **2022**, *920*, 165821.

(20) Wu, Y.; Liu, X.; Han, D.; Song, X.; Shi, L.; Song, Y.; Niu, S.; Xie, Y.; Cai, J.; Wu, S.; Kang, J.; Zhou, J.; Chen, Z.; Zheng, X.; Xiao, X.; Wang, G. Electron Density Modulation of NiCo2S4 Nanowires by Nitrogen Incorporation for Highly Efficient Hydrogen Evolution Catalysis. *Nat Commun* **2018**, *9*, 1425.

(21) Zhang, C.; Wang, X.; Song, K.; Chen, K.; Dai, S.; Wang, H.; Huang, M. Engineering Adjacent Fe3C as Proton-Feeding Centers to Single Fe Sites Enabling Boosted Oxygen Reduction Reaction Kinetics for Robust Zn-Air Batteries at High Current Densities. *Nano Res* **2023**, *16*, 9371–9378.

(22) Li, M.; Zhu, H.; Yuan, Q.; Li, T.; Wang, M.; Zhang, P.; Zhao, Y.; Qin, D.; Guo, W.; Lui, B.; Yang, X.; Liu, Y.; Pan, Y. Proximity Electronic Effect of Ni/Co Diatomic Sites for Synergistic Promotion of Electrocatalytic Oxygen Reduction and Hydrogen Evolution. *Adv Funct Mater* **2022**, *33*, 2210867.

(23) Qu, M.; Jiang, Y.; Yang, M.; Liu, S.; Guo, Q.; Shen, W.; Li, M.; He, R. Regulating Electron Density of NiFe-P Nanosheets Electrocatalysts by a Trifle of Ru for High-Efficient Overall Water Splitting. *Appl Catal B* **2020**, *263*, 118324.

(24) Jerigová, M.; Heske, J.; Kühne, T. D.; Tian, Z.; Tovar, M.; Odziomek, M.; López-Salas, N. C1N1 Thin Films from Guanine Decomposition Fragments. *Adv Mater Interfaces* **2023**, *10*, 2202061.

(25) Kossmann, J.; Heil, T.; Antonietti, M.; López-Salas, N. Guanine-Derived Porous Carbonaceous Materials: Towards C1N1. *ChemSusChem* **2020**, *13*, 6643–6650.

(26) Quílez-Bermejo, J.; García-Dalí, S.; Daouli, A.; Zitolo, A.; Canevesi, R.; Emo, M.; Izquierdo, M. T.; Badawi, M.; Celzard, A.; Fierro, V. Advanced Design of Metal Nanoclusters and Single Atoms Embedded in C1N1-Derived Carbon Materials for ORR, HER, and OER. *Adv Funct Mater* **2023**, *2300405*.

(27) Miller, T. S.; Belen-Jorge, A.; Suter, T. M.; Sella, A.; Corà, F.; McMillan, P. F. Carbon Nitrides: Synthesis and Characterization of a New Class of Functional Materials. *Physical Chemistry Chemical Physics* **2017**, *19*, 15613–15638.

(28) Quílez-Bermejo, J.; Morallón, E.; Cazorla-Amorós, D. Polyaniline-Derived N-Doped Ordered Mesoporous Carbon Thin Films: Efficient Catalysts towards Oxygen Reduction Reaction. *Polymers* **2020**, *12*, 2382.

(29) Kossmann, J.; Heil, T.; Antonietti, M.; López-Salas, N. Guanine-Derived Porous Carbonaceous Materials: Towards C1N1. *ChemSusChem* **2020**, *13*, 6643–6650.

(30) Tang, Y.; Wang, X.; Chen, J.; Wang, X.; Wang, D.; Mao, Z. PVP-Assisted Synthesis of g-C3N4-Derived N-Doped Graphene with Tunable Interplanar Spacing as High-Performance Lithium/Sodium Ions Battery Anodes. *Carbon* **2021**, *174*, 98–109.

(31) Ferrari, A. C.; Robertson, J. Interpretation of Raman Spectra of Disordered and Amorphous Carbon. *Phys. Rev. B* **2000**, *61*, 14095.

(32) Ferrari, A. C.; Meyer, J. C.; Scardaci, V.; Casiraghi, C.; Lazzeri, M.; Mauri, F.; Piscanec, S.; Jiang, D.; Novoselov, K. S.; Roth, S.; Geim, A. K. Raman Spectrum of Graphene and Graphene Layers $^{\mathrm{o}}$. *Phys Rev Lett* **2006**, *97*, 187401.

(33) López-Díaz, D.; López-Holgado, M.; García-Fierro, J. L.; Velázquez, M. M. Evolution of the Raman Spectrum with the Chemical Composition of Graphene Oxide. *J. Phys. Chem. C* **2017**, *121*, 20489–20497.

(34) López-Díaz, D.; Delgado-Notario, J. A.; Clericò, V.; Diez, E.; Dolores-Merchán, M.; Velázquez, M. M. Towards Understanding the Raman Spectrum of Graphene Oxide: The Effect of the Chemical Composition. *Coatings* **2020**, *10*, 524.

(35) Thompson, E.; Danks, A. E.; Bourgeois, L.; Schnepp, Z. Iron-Catalyzed Graphitization of Biomass. *Green Chemistry* **2015**, *17*, 551–556.

(36) Krishnakumar, V.; Prabavathi, N. Scaled Quantum Chemical Calculations and FTIR, FT-Raman Spectral Analysis of 2-Methylpyrazine. *Spectrochim Acta A Mol Biomol Spectrosc* **2009**, *72*, 743–747.

(37) Li, G.; Sheng, K.; Lei, Y.; Yang, J.; Chen, Y.; Guo, X.; Chen, G.; Chang, B.; Wu, T.; Wang, X. Facile Synthesis of Fe3C-Dominated Fe/Fe3C/FeN0.0324 Multiphase Nanocrystals Embedded in Nitrogen-Modified Graphitized Carbon as Efficient PH-Universal Catalyst for Oxygen Reduction Reaction and Zinc-Air Battery. *Chemical Engineering Journal* **2023**, *451*, 138823.

(38) Tan, H.; Li, Y.; Kim, J.; Takei, T.; Wang, Z.; Xy, X.; Wang, J.; Bando, Y.; Kang, Y. M.; Tang, J.; Yamauchi, Y. Sub-50 Nm Iron–Nitrogen-Doped Hollow Carbon Sphere-Encapsulated Iron Carbide Nanoparticles as Efficient Oxygen Reduction Catalysts. *Advanced Science* **2018**, *5*, 1800120.

(39) Quílez-Bermejo, J.; González-Gaitán, C.; Morallón, E.; Cazorla-Amorós, D. Effect of Carbonization Conditions of Polyaniline on Its Catalytic Activity towards ORR. Some Insights about the Nature of the Active Sites. *Carbon* **2017**, *119*, 62–71. https://doi.org/10.1016/j.carbon.2017.04.015.

(40) Quílez-Bermejo, J.; Pérez-Rodríguez, S.; Canevesi, R. L. S.; Torres, D.; Morallón, E.; Cazorla-Amorós, D.; Celzard, A.; Fierro, V. Easy Enrichment of Graphitic Nitrogen to Prepare Highly Catalytic Carbons for Oxygen Reduction Reaction. *Carbon* **2022**, *196*, 708–717.

(41) Quílez-Bermejo, J.; Morallón, E.; Cazorla-Amorós, D. On the Deactivation of N-Doped Carbon Materials Active Sites during Oxygen Reduction Reaction. *Carbon* **2022**, *189*, 548–560.

(42) Tian, Y.; Wu, Z.; Li, M.; Sun, Q.; Chen, H.; Yuan, D.; Deng, D.; Johannessen, B.; Wang, Y.; Zhong, Y.; Xu, L.; Lu, J.; Zhang, S. Atomic Modulation and Structure Design of Fe–N4 Modified Hollow Carbon Fibers with Encapsulated Ni Nanoparticles for Rechargeable Zn–Air Batteries. *Adv Funct Mater* **2022**, *32*, 2209273.

(43) Quílez-Bermejo, J.; Morallón, E.; Cazorla-Amorós, D. Metal-Free Heteroatom-Doped Carbon-Based Catalysts for ORR. A Critical Assessment about the Role of Heteroatoms. *Carbon* **2020**, *165*, 434–454.

(44) Park, S.; Her, M.; Shin, H.; Hwang, W.; Sung, Y. E. Maximizing the Active Site Densities of Single-Atomic Fe–N–C Electrocatalysts for High-Performance Anion Membrane Fuel Cells. *ACS Appl Energy Mater* **2021**, *4*, 1459–1466.

(45) Woo, J.; Yang, S. Y.; Sa, Y. J.; Choi, W. Y.; Lee, M. H.; Lee, H. W.; Shin, T. J.; Kim, T. Y.; Joo, S. H. Promoting Oxygen Reduction Reaction Activity of Fe–N/C Electrocatalysts by Silica-Coating-Mediated Synthesis for Anion-Exchange Membrane Fuel Cells. *Chemistry of Materials* **2018**, *30*, 6684–6701.

(46) Lilloja, J.; Kibena-Poldsepp, E.; Sarapuu, A.; Kodali, M.; Chen, Y.; Asset, T.; Kaarik, M.; Merisalu, M.; Paiste, P.; Aruvali, J.; Teshchalov, A.; Rahn, M.; Leis, J.; Sammerlselg, V.; Holdcroft, S.; Atanassov, P.; Tammeveski, K. Cathode Catalysts Based on Cobalt- and Nitrogen-Doped Nanocarbon Composites for Anion Exchange Membrane Fuel Cells. *ACS Appl Energy Mater* **2020**, *3*, 5375–5384.

(47) Pei, Y.; Zhu, W.; Yue, R.; Yao, J.; Liu, X.; Wang, L.; Zhang, J.; Yin, Y.; Guiver, M. D. Fine Adjustment of Catalyst Agglomerate for the Controllable Construction of Co/Fe–N–C Catalyst Layers. *J Power Sources* **2023**, *566*, 232904.

(48) Lilloja, J.; Kibena-Poldsepp, E.; Sarapuu, A.; Kaarik, M.; Kozlova, J.; Paiste, P.; Kikas, A.; Treshchalov, A.; Leis, J.; Tamm, A.; Kisand, V.; Holdcroft, S.; Tammeveski, K. Transition Metal and Nitrogen-Doped Mesoporous Carbons as Cathode Catalysts for Anion-Exchange Membrane Fuel Cells. *Appl Catal B* **2022**, *306*, 121113.

(49) Sa, Y. J.; Seo, D. J.; Woo, J.; Lim, J. T.; Cheon, J. Y.; Yang, S. Y.; Lee, J. M.; Kang, D.; Shin, T. J.; Shin, H. S.; Jeong, H. Y.; Kim, C. S.; Kim, M. G.; Kim, T. Y.; Joo, S. H. A General Approach to Preferential Formation of Active Fe–Nx Sites in Fe–N/C Electrocatalysts for Efficient Oxygen Reduction Reaction. *Journal of American Chemical Society* **2016**, *138*, 15046–15056.

(50) Kang, G. S.; Jang, J. H.; Son, S. Y.; Lee, Y. K.; Lee, D. C.; Yoo, S. J.; Lee, S.; Joh, H. I. Pyrrolic N Wrapping Strategy to Maximize the Number of Single-Atomic Fe-Nx Sites for Oxygen Reduction Reaction. *J Power Sources* **2022**, *520*, 230904.

(51) Rauf, M.; Wang, J.; Handschih-Wang, S.; Zhou, Z.; Iqbal, W.; Khan, S. A.; Zhuang, L.; Ren, X.; Li, Y.; Sun, S. Highly Stable N-Containing Polymer-Based Fe/Nx/C Electrocatalyst for Alkaline Anion Exchange Membrane Fuel Cell Applications. *Progress in Natural Science: Materials International* **2022**, *32*, 27–33.

(52) Liu, J.; Wang, J.; Zhang, L.; Fan, C.; Zhou, X.; Zhang, B.; Cui, X.; Wang, J.; Cheng, Y.; Sun, S.; Jiang, L. Axial Ligand Promoted Phosphate Tolerance of an Atomically Dispersed Fe Catalyst towards the Oxygen Reduction Reaction. *J Mater Chem A Mater* **2022**, *10*, 16722–16729.

(53) Hossen, M. M.; Artyushkova, K.; Atanassov, P.; Serov, A. Synthesis and Characterization of High Performing Fe-N-C Catalyst for Oxygen Reduction Reaction (ORR) in Alkaline Exchange Membrane Fuel Cells. *J Power Sources* **2018**, *375*, 214–221.

(54) Lilloja, J.; Mooste, M.; Kibena-Poldsepp, E.; Sarapuu, A.; Zulevi, B.; Kikas, A.; Piirsoo, H. M.; Tamm, A.; Kisand, V.; Holdcroft, S.; Serov, A.; Tammeveski, K. Mesoporous Iron-Nitrogen Co-Doped Carbon Material as Cathode Catalyst for the Anion Exchange Membrane Fuel Cell. *Journal of Power Sources Advances* **2021**, *8*, 100052.

(55) Praats, R.; Kaarik, M.; Kikas, A.; Kisand, V.; Aruvali, J.; Paiste, P.; Merisalu, M.; Leis, J.; Sammelselg, V.; Zagal, J. H.; Holdcroft, S.; Nakashima, N.; Tammeveski, K. Electrocatalytic Oxygen Reduction Reaction on Iron Phthalocyanine-Modified Carbide-Derived Carbon/Carbon Nanotube Composite Electrocatalysts. *Electrochim Acta* **2020**, *334*, 135575.

(56) Freitas, W. d. S.; D'Epifanio, A.; Vecchio, C. Lo; Gatto, I.; Baglio, V.; Ficca, V. C. A.; Placidi, E.; Mecheri, B. Tailoring MOF Structure via Iron Decoration to Enhance ORR in Alkaline Polymer Electrolyte Membrane Fuel Cells. *Chemical Engineering Journal* **2023**, *465*, 142987.

(57) Karuppannan, M.; Park, J. E.; Bae, Y. E.; Cho, Y. H.; Kwon, O. J. A Nitrogen and Fluorine Enriched Fe/Fe3C@C Oxygen Reduction Reaction Electrocatalyst for Anion/Proton Exchange Membrane Fuel Cells. *Nanoscale* **2020**, *12*, 2542–2554.

(58) Mashkani, F. A.; Gharibi, H.; Amani, M.; Zhiani, M.; Morsali, A. A Novel Electrocatalyst Based on Fe-ZIF-PPY Nanocomposite for Oxygen Reduction Reaction in Air-Breathing Direct-Ethanol Fuel Cell. *Appl Surf Sci* **2022**, *548*, 152529.

(59) Shen, L.; Ying, J.; Ozoemena, K. I.; Janiak, C.; Yang, X. Y. Confinement Effects in Individual Carbon Encapsulated Nonprecious Metal-Based Electrocatalysts. *Adv Funct Mater* **2022**, *32*, 2110851.

(60) Deng, J.; Ren, P.; Deng, D.; Bao, X. Enhanced Electron Penetration through an Ultrathin Graphene Layerfor Highly Efficient Catalysis of the Hydrogen Evolution Reaction. *Angewandte Chemie - International Edition* **2015**, *54*, 2100–2104.

(61) Shen, H.; Thomas, T.; Rasaki, S. A.; Saad, A.; Hu, C.; Wang, J.; Yang, M. Oxygen Reduction Reactions of Fe-N-C Catalysts: Current Status and the Way Forward. *Electrochemical Energy Reviews* **2019**, 252–276.

(62) Sun, M.; Chen, C.; Wu, M.; Zhou, D.; Sun, Z.; Fan, J.; Chen, W.; Li, Y. Rational Design of Fe-N-C Electrocatalysts for Oxygen Reduction Reaction: From Nanoparticles to Single Atoms. *Nano Res* **2022**, *15*, 1753–1778.

(63) Deng, J.; Yu, L.; Deng, D.; Chen, X.; Yang, F.; Bao, X. Highly Active Reduction of Oxygen on a FeCo Alloy Catalyst Encapsulated in Pod-like Carbon Nanotubes with Fewer Walls. *J Mater Chem A Mater* **2013**, *1*, 14868.